Trapped fractional charges at bulk defects in topological insulators

https://doi.org/10.1038/s41586-020-03117-3

Received: 23 April 2020

Accepted: 22 October 2020

Published online: 20 January 2021

Check for updates

Christopher W. Peterson[1], Tianhe Li[2], Wentao Jiang[1], Taylor L. Hughes[2] & Gaurav Bahl[3]✉

Topological crystalline insulators (TCIs) can exhibit unusual, quantized electric phenomena such as fractional electric polarization and boundary-localized fractional charge[1–6]. This quantized fractional charge is the generic observable for identification of TCIs that lack clear spectral features[5–7], including ones with higher-order topology[8–11]. It has been predicted that fractional charges can also manifest where crystallographic defects disrupt the lattice structure of TCIs, potentially providing a bulk probe of crystalline topology[10,12–14]. However, this capability has not yet been confirmed in experiments, given that measurements of charge distributions in TCIs have not been accessible until recently[11]. Here we experimentally demonstrate that disclination defects can robustly trap fractional charges in TCI metamaterials, and show that this trapped charge can indicate non-trivial, higher-order crystalline topology even in the absence of any spectral signatures. Furthermore, we uncover a connection between the trapped charge and the existence of topological bound states localized at these defects. We test the robustness of these topological features when the protective crystalline symmetry is broken, and find that a single robust bound state can be localized at each disclination alongside the fractional charge. Our results conclusively show that disclination defects in TCIs can strongly trap fractional charges as well as topological bound states, and demonstrate the primacy of fractional charge as a probe of crystalline topology.

Topological insulators are materials characterized by quantized topological invariants that are defined with respect to the symmetries of their gapped bulk Hamiltonian[15–17]. The most well known class of topological insulators are those that have robust in-gap states on boundaries one dimension lower than the bulk, and which are protected by local symmetries, such as time reversal[18–21]. The robust boundary states provide a characteristic spectral signature for experimental identification. In addition to local symmetries, crystalline symmetries can likewise protect topological invariants such as a quantized electric polarization[22–24]. However, the topological crystalline insulators (TCIs) (we note that in this paper, we refer to any system with non-trivial topological crystalline invariants as a TCI, including both phases described as obstructed atomic limits and phases defined as topological insulators according to the topological quantum chemistry paradigm[25]) protected by these symmetries may not always manifest spectral features in their bulk bandgap, as crystalline symmetries in many cases protect only the degeneracy of boundary-localized states, and do not restrict their energy[10,11].

Instead, TCIs lacking robust spectral features can be identified by, for example, the quantized fractional charge that manifests at their boundaries[1–6,24,26], including the higher-order TCIs, which manifest fractional charge at boundaries with higher co-dimension, such as corners in two dimensions[8,10,11,27]. Crystallographic defects that break certain crystalline symmetries, such as disclinations (defects of rotation symmetry), are expected to also trap fractional charges[10,13,14]. This trapped fractional charge thus serves as a generic bulk probe of crystalline topology, enabling crystalline insulators to be characterized independently from their boundary termination. In rotationally symmetric TCIs, the fractional charge Q (in units of elementary charge e) trapped by a disclination generically satisfies[10,14,28,29]

$$Q = \frac{\Omega}{2\pi}\eta + \sum_{i,j=1,2} \epsilon_{ij} B_i P_j \ \text{modulo}\ 1, \tag{1}$$

where the Frank angle Ω and the Burgers vector $\mathbf{B}$ characterize the topological class of the defect, and the electric polarization $\mathbf{P}$ and Wannier representation index η capture the topology of the TCI's band structure (ϵ_{ij} is the Levi–Civita symbol, where i and j index the dimensions; see Methods for a detailed explanation of these quantities). However, the experimental confirmation of this relation has remained elusive as the measurements of the charge distribution within insulators have not been previously accessible.

Recently, an equivalent of boundary-localized fractional charge, the integrated mode density over a given frequency range (see Methods for details), has been measured experimentally in TCI metamaterials[11]. Using this measurement method, here we report the experimental observation of quantized fractional mode density in units of 1/4 trapped by two different disclination defects in a C_4-symmetric higher-order topological (crystalline) insulator (HOTI) metamaterial, one with a negative Frank angle $\Omega = -90°$ and one with a positive Frank angle $\Omega = +90°$,

[1]Department of Electrical and Computer Engineering, University of Illinois at Urbana-Champaign, Urbana, IL, USA. [2]Department of Physics, Institute for Condensed Matter Theory, University of Illinois at Urbana-Champaign, Urbana, IL, USA. [3]Department of Mechanical Science and Engineering, University of Illinois at Urbana-Champaign, Urbana, IL, USA. ✉e-mail: bahl@illinois.edu

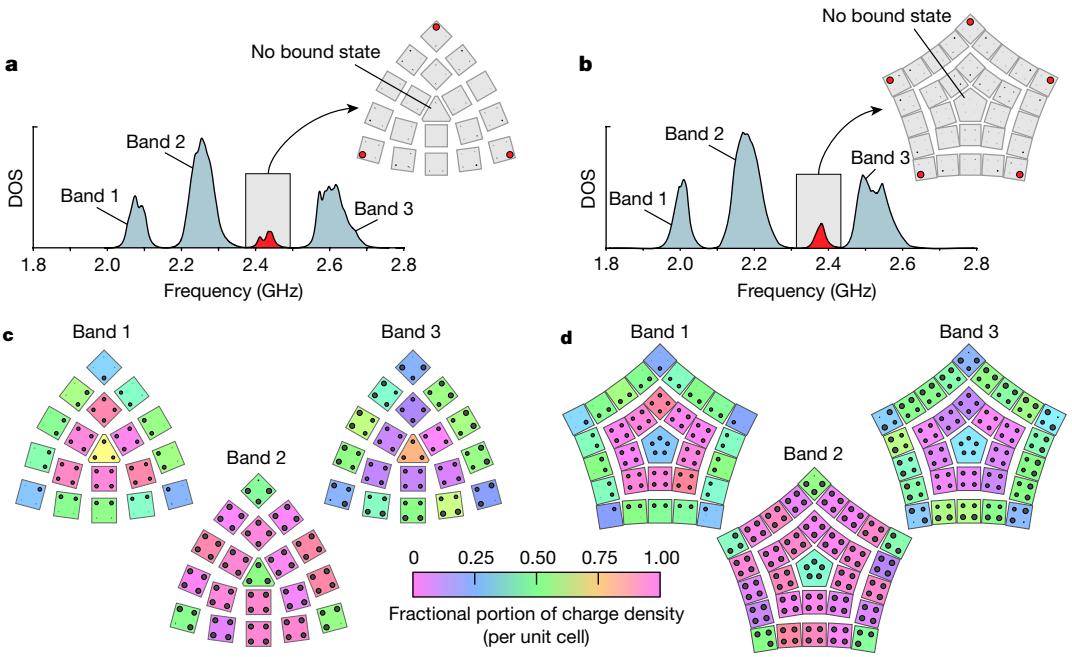

Fig. 1 | Measurement of trapped fractional mode density. a, Measured DOS for the C_3-symmetric board. The highlighted in-gap states are localized to the three corners, with no in-gap state at the disclination core. **b**, Same as **a** but for the C_5-symmetric board, which has five in-gap corner states. **c**, Measured mode density per unit cell in each of the three bands of the C_3-symmetric board. The colour of each unit cell indicates the fractional portion of mode density in that cell, and the area of each dot is proportional to the mode density of the corresponding resonator. Here the central unit cell has approximately 3/4 fractional mode density in bands 1 and 3. **d**, Same as **c** but for the C_5-symmetric board. Here the central unit cell has approximately 1/4 fractional mode density in bands 1 and 3. Detailed versions of **c** and **d** showing the total mode density per unit cell are available as Extended Data Figs. 7, 8.

as shown in Fig. 1 (see Methods for details on disclination defects and the HOTI metamaterial). Although fractional mode density is typically associated with topological bound states[11], we observe that no topological states are trapped by the disclinations when the fractional mode density lies within the defective central/core unit cells. For each case, we then show that a local deformation around the disclination core reveals an odd number of in-gap topological states trapped by each disclination defect.

Experimental results

To characterize the fabricated metamaterials, we first measure the spectral density of states (DOS) of each site (each resonator) individually using a network analyser reflection measurement (Methods). The total DOS spectrum, calculated by summing over all sites, is shown in Fig. 1a, b for the C_3- and C_5-symmetric metamaterials, respectively. As both are based on the same tight-binding Hamiltonian and differ only in the Frank angle of their disclination defect, we expect, and indeed find, that the spectral DOS are nearly identical. For both insulators, we measure three large, well-defined bands and a small number of states within the largest bandgap. The in-gap states are strongly localized to the materials' corners (Fig. 1a, b) and lie within the same unit cell as a 1/4 fractional mode density (Fig. 1c, d), indicating that these are the topological corner states of the HOTI[11]. Later, we will show that the fractional charge at the disclination core can also be associated with topological bound states, although these states are missing when the fractional mode density is within the defective unit cell at the disclination core, as in Fig. 1a, b. We note that a small on-site potential is added to the corner sites to shift these corner states into the bulk bandgap, otherwise these states would be obscured by the bulk bands.

Although the DOS spectra of the ideal tight-binding Hamiltonians that we implement are symmetric, the measured spectra are asymmetric for two main reasons. First, chiral symmetry is broken in the fabricated metamaterials because the capacitive coupling elements effectively increase the electrical length of the resonators, thereby decreasing their resonance frequencies. As the bulk resonators have more connections than those at the edges and corners, their resonance frequencies are shifted by a greater amount[11]. As a result, the two edge bands are observed to overlap with the two higher-frequency bulk bands. Second, the capacitive coupling is intrinsically frequency asymmetric because the electrical impedance of a capacitor is inversely proportional to frequency. This causes the coupling rate between resonators to increase with frequency, meaning that the bands as well as the bandgaps become wider at higher frequencies. However, this does not affect the topology of the metamaterials as it does not break the crystalline symmetry or close the bandgap (as the strong and weak coupling rates increase in the same proportion), such that it is a continuous deformation of an ideal system and cannot change the fractional features.

We now shift focus to the spatial distribution of mode density within the three large bands, concentrating on the fractional part. The spatially resolved mode densities for each band of the C_3- and C_5-symmetric metamaterials, which have an identical C_4-symmetric unit cell structure, are shown in Fig. 1c, d, respectively. As there are no energetic filling rules in these systems, we can consider the mode density distribution of each band separately. In the lowest and highest frequency bands, the edge unit cells have a fractional mode density of approximately 1/2, and each corner unit cell carries about 1/4 fractional mode density. The central band of this HOTI has identical density features to the other bands but is doubly degenerate, which doubles the mode density when compared with the singly degenerate bands[11]. As such, in the central band, only the corner unit cells have a fractional mode density (a value of 1/2). In the bulk unit cells, the mode density takes an integer value for all bands, except in the central unit cell where the disclination occurs. For the negative disclination ($\Omega = -90°$), this defective central unit cell has a fractional mode density of 3/4 in the singly degenerate bands, as predicted by the gluing picture in Fig. 1. In contrast, the positive disclination ($\Omega = +90°$) generates a fractional mode density of 1/4 in the

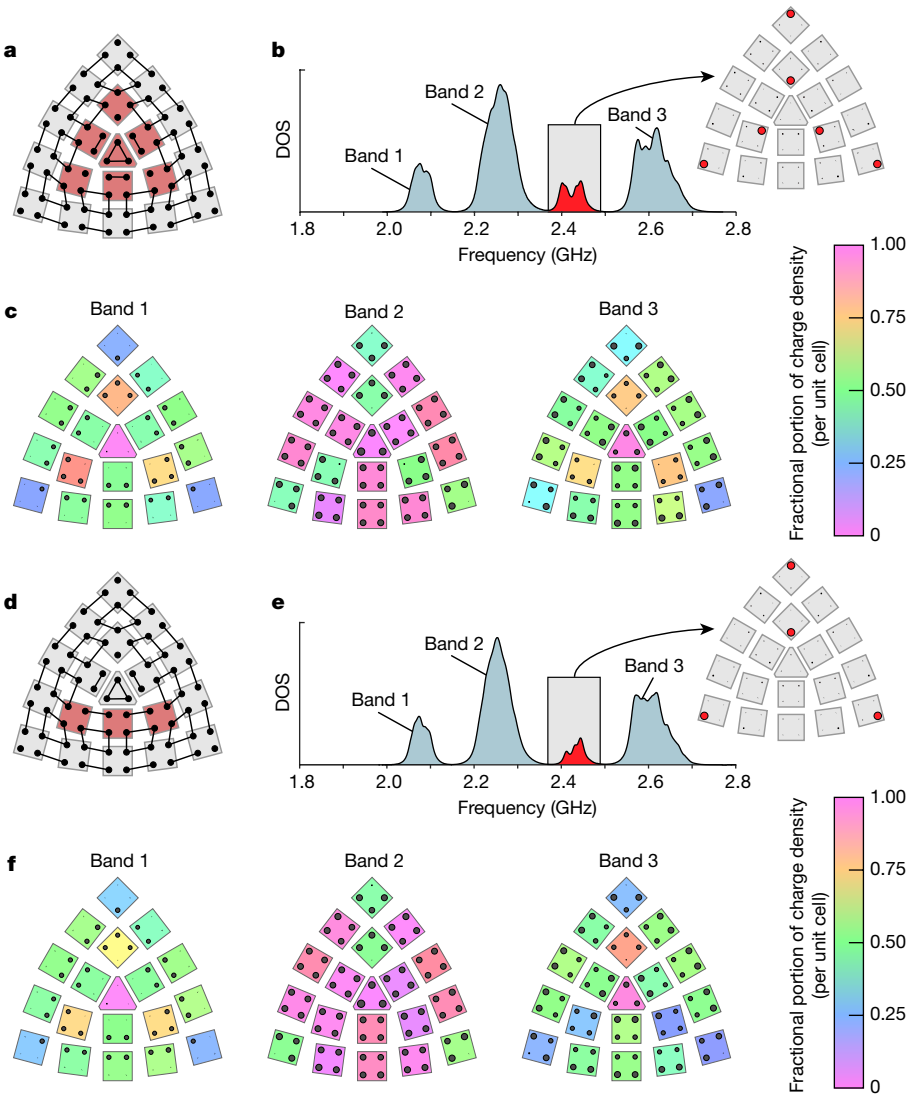

Fig. 2 | Local deformation reveals trapped in-gap state (C_3). **a**, Deformed C_3-symmetric lattice with trivial central unit cell (only highlighted unit cells are deformed). **b**, Measured DOS for the deformed lattice in **a**. Highlighted in-gap states are localized to the original exterior corners, plus three interior corners. **c**, Measured mode density for each of the three bands shown in **b**. The central unit cell now has an integer mode density and surrounding unit cells host fractional mode density. **d**–**f**, Same as **a**–**c**, but the lattice is further deformed, breaking C_3 rotation symmetry, such that two of the interior corner states are gapped out. Highlighted unit cells in **d** are deformed from **a**. The fractional mode density in bands 2 and 3 changes in these unit cells due to the deformation. Detailed versions of **c** and **f** showing the total mode density per unit cell are available as Extended Data Fig. 9.

defective unit cell for these bands, which is also expected. We note that these trapped charges are also doubled in the twice-degenerate central band. To support these experimental results, we have also performed tight-binding simulations of both disclinations in larger finite systems, available in Methods.

Trapped topological bound states

Having established the existence of trapped fractional mode density at the disclination cores, we now demonstrate its relationship to trapped topological bound states. As the systems that we study do not have chiral symmetry, the topological bound states are not pinned to the zero-energy level, instead their energy directly corresponds to the energy of the site where they are localized (see discussion in Methods). Boundary-induced fractional mode density has been shown to be associated with such topological boundary states[11], as exemplified by the corner unit cells of both insulators in Fig. 1. However, for the reason detailed below, we expect that the association between fractional mode density and topological states only holds when all unit cells in the system contain the same number of sites/modes. The fractional mode density is a collective property of the bulk and cannot be changed by deformations, even relatively violent ones that locally add or remove sites, as we show in Methods, but such deformations can remove topological bound states. This property is clearly evident in the zero-correlation-length limit, where the weak coupling rate within unit cells goes to zero. In this limit, topological bound states will lie entirely on sites that are decoupled from the rest of the system. As such, removing these sites will also remove the bound states. As the zero-correlation-length limit can always be deformed into an arbitrary finite correlation length without closing the bandgap or changing the number of bound states, this property is also true in general (see discussion in Methods).

In our fabricated metamaterials, the unit cell contains four sites, but the defective central unit cell has three sites in the C_3-symmetric insulator and five in the C_5-symmetric insulator. Hence, we do not expect a conventional association between the trapped fractional mode density and topological bound states. This is supported by the measurements in Fig. 1, which show no evidence of bound states at the disclinations—the spectrum of each site in the bulk is identically gapped, leaving no room for a localized bound state. However, although neither of these central unit cells hosts topological bound states, we will now show that such states can be generated near the disclination core by deformations that shift the fractional charge from the defective unit cell into the surrounding intact unit cells. We note that these newly generated bound states are not created by adding or removing sites from the system, but naturally appear due to the topological nature of the disclination defects when the defective unit cell at the core is transitioned into a topologically trivial phase.

We first deform the central unit cell in both metamaterials such that the sites within it are strongly coupled to each other and are weakly

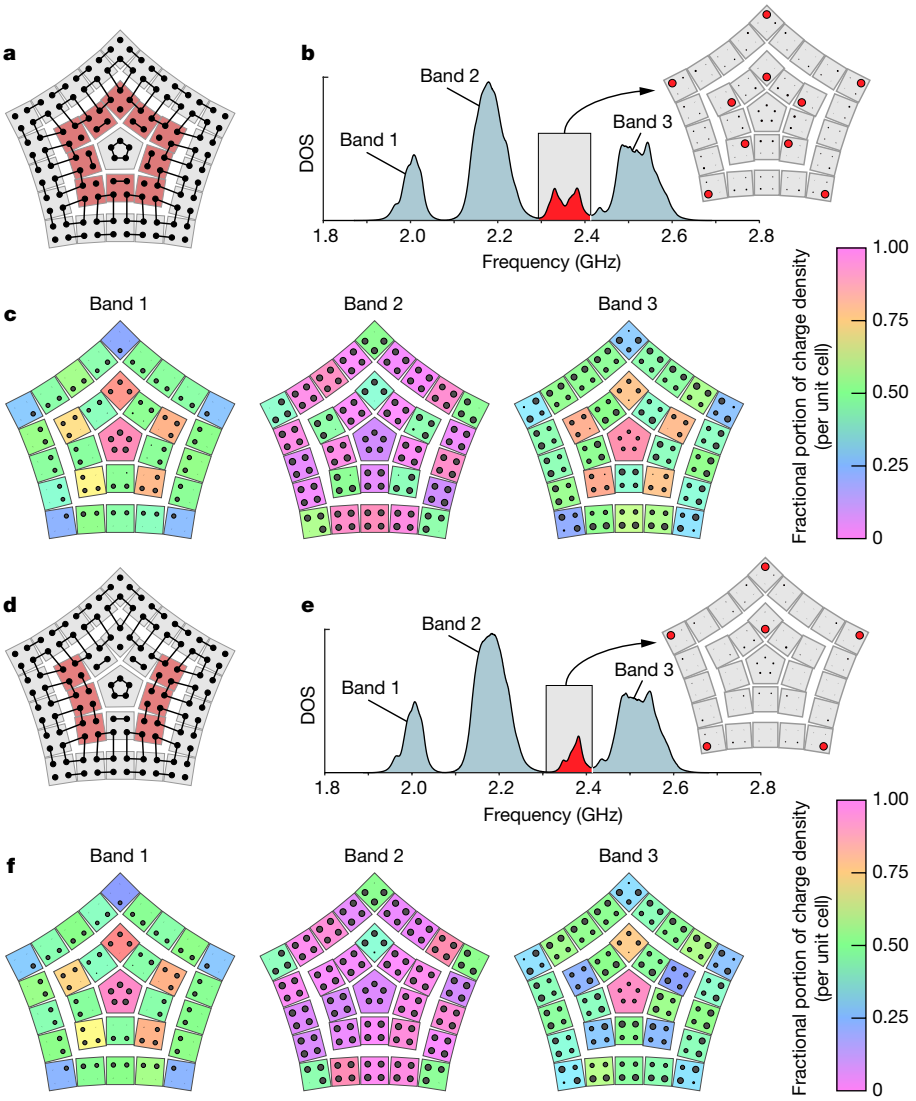

Fig. 3 | Local deformation reveals trapped in-gap state (C_5). a–f, Same as Fig. 2 but for the C_5-symmetric insulator. Detailed versions of **c** and **f** showing the total mode density per unit cell are available as Extended Data Fig. 10.

coupled to sites in neighbouring unit cells. This is equivalent to putting only the central unit cell in a topologically trivial phase. We also deform the unit cells immediately adjacent to the disclination such that they form an interior boundary, similar to the exterior boundary, around the central unit cell. These deformations do not break the global rotation symmetry, as illustrated in the schematics of the deformed C_3- and C_5-symmetric insulators shown in Figs. 2a, 3a, respectively. After the deformations are complete, we again measure the spectral DOS of each site to find the spatial mode density, which is shown in Figs. 2c, 3c for the C_3- and C_5-symmetric materials, respectively.

As the central unit cell of both metamaterials is now topologically trivial, the mode density in this unit cell takes an integer value in all three bands. We find that the fractional mode density that was previously trapped at the disclination has symmetrically split and moved to the interior boundary, with 3/4 charges on each interior corner and 1/2 charges along the interior edge in the singly degenerate bands. In the C_3-symmetric insulator, the original 3/4 mode density splits, creating three unit cells with 3/4 mode density and three with 1/2 mode density (total 3 and 3/4). Likewise, the C_5-symmetric insulator, which originally had a 1/4 mode density in the centre unit cell, contains five unit cells with 3/4 mode density and five with 1/2 mode density after the deformation (total 6 and 1/4). We note that the total fractional part of the mode density (that is, the mode density modulo 1) in each sector remains constant for each of the bands, even after these deformations, as we do not break the global rotation symmetry and the bulk bandgap does not close away from the core.

In addition to the splitting of fractional mode density, this deformation also results in three (or five) additional topological bound states within the bandgap. These states are located at the interior corners of the system around the trivial central unit cell, as shown in Figs. 2b, 3b, respectively. We note that there are an odd number of bound states that emerge in both deformed systems, which is required by the global C_3 or C_5 rotation symmetry as the bound states must either lie at the rotation centre or be identically distributed in each of the three (or five) symmetric sectors. These states are not protected against deformations that break these symmetries; however, even if the rotation symmetry is broken, the topologically non-trivial nature of these disclination defects ensures that one bound state always survives (except in the cases where the unit cell is defective and broken, as discussed above). We demonstrate this property by breaking the rotation symmetry through further local deformation of both metamaterial samples, as illustrated schematically in Figs. 2d, 3d. Note that only the highlighted unit cells are deformed. This deformation strongly couples all but one of the disclination-induced bound states in pairs. The coupled states

become gapped and no longer lie within the bandgap (Figs. 2e, 3e), instead splitting such that they enter both the central and upper bulk bands. This is accompanied by an increase of 1/2 fractional mode density in each of these bands within the highlighted interior-corner unit cells (Figs. 2f, 3f).

We note that this increase is only possible because the rotation symmetry is broken by the deformation, and the fractional mode density in each sector is no longer symmetry protected. Following these deformations, a single topological bound state remains within the bulk of each deformed insulator, as shown in Figs. 2e, 3e. Although only a single bound state remains, the association between fractional mode density and topological bound states discussed above still holds in these cases. As the rotation symmetry is broken, this association no longer applies to each symmetric sector but to the total disclination-induced fractional mode density. Thus, the singular bound states in the triangular and pentagonal metamaterials can be associated with the trapped 3/4 and 1/4 fractional mode densities, respectively.

Potential applications

Topological bound states trapped by disclinations could prove useful for a variety of engineering applications as these defects can lie deep within the bulk away from the material boundaries. For example, topological pumps have been shown to be capable of robustly transferring vibrational energy between topological bound states[30]. Similar pumping processes could be used to transfer energy into bound states trapped at disclinations deep within the bulk of a material, where the energy could be safely stored without radiative decay due to the surrounding insulator. Topological edge states have also been shown to exhibit desirable properties for laser applications, including high-power single-mode lasing, robustness against fabrication defects and high slope efficiency[31–33]. Defect-bound topological states could be used to create similar topological lasers (especially in three-dimensional HOTIs), which could prove less sensitive to external noise and radiative loss as they are not fixed to a surface. Furthermore, experiments on certain types of nonlinear topological insulators have shown that topological bound states can be used to drive topological transitions[34,35], including in HOTIs[36]. Our results provide an important first step to these applications, demonstrating that topological features trapped at disclinations can be identified through measurement of charge density and, if necessary, revealed through local deformations.

Fractional charge trapped at lattice defects could potentially also be used to identify crystalline topology in solid-state materials, where the local DOS can be measured through, for example, scanning tunnelling spectroscopy[37,38] or using a scanning single electron transistor[39], but boundary-localized fractional charges may be more challenging to observe. In addition, if one can tune a transition between the topologically non-trivial and trivial phases in situ, it may be possible to measure a precise current associated with the accumulation of fractional charge by tracking the change in Coulomb blockade peaks using a single-electron transistor device[40].

Online content

Any methods, additional references, Nature Research reporting summaries, source data, extended data, supplementary information, acknowledgements, peer review information; details of author contributions and competing interests; and statements of data and code availability are available at https://doi.org/10.1038/s41586-020-03117-3.

1. Zak, J. Berry's phase for energy bands in solids. *Phys. Rev. Lett.* **62**, 2747–2750 (1989).
2. Vanderbilt, D. & King-Smith, R. D. Electric polarization as a bulk quantity and its relation to surface charge. *Phys. Rev. B* **48**, 4442–4455 (1993).
3. King-Smith, R. D. & Vanderbilt, D. Theory of polarization of crystalline solids. *Phys. Rev. B* **47**, 1651–1654 (1993).
4. Resta, R. Macroscopic polarization in crystalline dielectrics: the geometric phase approach. *Rev. Mod. Phys.* **66**, 899–915 (1994).
5. Hughes, T. L., Prodan, E. & Bernevig, B. A. Inversion-symmetric topological insulators. *Phys. Rev. B* **83**, 245132 (2011).
6. Turner, A. M., Zhang, Y., Mong, R. S. K. & Vishwanath, A. Quantized response and topology of magnetic insulators with inversion symmetry. *Phys. Rev. B* **85**, 165120 (2012).
7. van Miert, G. & Ortix, C. Excess charges as a probe of one-dimensional topological crystalline insulating phases. *Phys. Rev. B* **96**, 235130 (2017).
8. Benalcazar, W. A., Bernevig, B. A. & Hughes, T. L. Quantized electric multipole insulators. *Science* **357**, 61–66 (2017).
9. Benalcazar, W. A., Bernevig, B. A. & Hughes, T. L. Electric multipole moments, topological multipole moment pumping, and chiral hinge states in crystalline insulators. *Phys. Rev. B* **96**, 245115 (2017).
10. Benalcazar, W. A., Li, T. & Hughes, T. L. Quantization of fractional corner charge in C_n-symmetric higher-order topological crystalline insulators. *Phys. Rev. B* **99**, 245151 (2019).
11. Peterson, C. W., Li, T., Benalcazar, W. A., Hughes, T. L. & Bahl, G. A fractional corner anomaly reveals higher-order topology. *Science* **368**, 1114–1118 (2020).
12. van Miert, G. & Ortix, C. Dislocation charges reveal two-dimensional topological crystalline invariants. *Phys. Rev. B* **97**, 201111 (2018).
13. Liu, S., Vishwanath, A. & Khalaf, E. Shift insulators: rotation-protected two-dimensional topological crystalline insulators. *Phys. Rev. X* **9**, 031003 (2019).
14. Li, T., Zhu, P., Benalcazar, W. A. & Hughes, T. L. Fractional disclination charge in two-dimensional C_n-symmetric topological crystalline insulators. *Phys. Rev. B* **101**, 115115 (2020).
15. Schnyder, A. P., Ryu, S., Furusaki, A. & Ludwig, A. W. Classification of topological insulators and superconductors in three spatial dimensions. *Phys. Rev. B* **78**, 195125 (2008).
16. Hasan, M. Z. & Kane, C. L. Topological insulators. *Rev. Mod. Phys.* **82**, 3045–3067 (2010).
17. Qi, X.-L. & Zhang, S.-C. Topological insulators and superconductors. *Rev. Mod. Phys.* **83**, 1057–1110 (2011).
18. Kane, C. L. & Mele, E. J. Quantum spin Hall effect in graphene. *Phys. Rev. Lett.* **95**, 226801 (2005).
19. Bernevig, B. A., Hughes, T. L. & Zhang, S.-C. Quantum spin Hall effect and topological phase transition in HgTe quantum wells. *Science* **314**, 1757–1761 (2006).
20. Fu, L., Kane, C. L. & Mele, E. J. Topological insulators in three dimensions. *Phys. Rev. Lett.* **98**, 106803 (2007).
21. Moore, J. E. & Balents, L. Topological invariants of time-reversal-invariant band structures. *Phys. Rev. B* **75**, 121306 (2007).
22. Teo, J. C. Y., Fu, L. & Kane, C. L. Surface states and topological invariants in three-dimensional topological insulators: application to $Bi_{1-x}Sb_x$. *Phys. Rev. B* **78**, 045426 (2008).
23. Fu, L. Topological crystalline insulators. *Phys. Rev. Lett.* **106**, 106802 (2011).
24. Fang, C., Gilbert, M. J. & Bernevig, B. A. Bulk topological invariants in noninteracting point group symmetric insulators. *Phys. Rev. B* **86**, 115112 (2012).
25. Bradlyn, B. et al. Topological quantum chemistry. *Nature* **547**, 298–305 (2017); correction **582**, E14 (2020).
26. Su, W. P., Schrieffer, J. R. & Heeger, A. J. Solitons in polyacetylene. *Phys. Rev. Lett.* **42**, 1698–1701 (1979).
27. van Miert, G. & Ortix, C. Higher-order topological insulators protected by inversion and rotoinversion symmetries. *Phys. Rev. B* **98**, 081110 (2018).
28. Teo, J. C. Y. & Hughes, T. L. Existence of Majorana-fermion bound states on disclinations and the classification of topological crystalline superconductors in two dimensions. *Phys. Rev. Lett.* **111**, 047006 (2013).
29. Benalcazar, W. A., Teo, J. C. Y. & Hughes, T. L. Classification of two-dimensional topological crystalline superconductors and Majorana bound states at disclinations. *Phys. Rev. B* **89**, 224503 (2014).
30. Grinberg, I. H. et al. Robust temporal pumping in a magneto-mechanical topological insulator. *Nat. Commun.* **11**, 974 (2020).
31. Bandres, M. A. et al. Topological insulator laser: experiments. *Science* **359**, eaar4005 (2018).
32. Harari, G. et al. Topological insulator laser: theory. *Science* **359**, eaar4003 (2018).
33. St-Jean, P. et al. Lasing in topological edge states of a one-dimensional lattice. *Nat. Photon.* **11**, 651–656 (2017).
34. Hadad, Y., Khanikaev, A. B. & Alù, A. Self-induced topological transitions and edge states supported by nonlinear staggered potentials. *Phys. Rev. B* **93**, 155112 (2016).
35. Hadad, Y., Soric, J. C., Khanikaev, A. B. & Alù, A. Self-induced topological protection in nonlinear circuit arrays. *Nat. Electron.* **1**, 178–182 (2018).
36. Zangeneh-Nejad, F. & Fleury, R. Nonlinear second-order topological insulators. *Phys. Rev. Lett.* **123**, 053902 (2019).
37. Nayak, A. K. et al. Resolving the topological classification of bismuth with topological defects. *Sci. Adv.* **5**, eaax6996 (2019).
38. Avraham, N. et al. Visualizing coexisting surface states in the weak and crystalline topological insulator Bi_2TeI. *Nat. Mater.* **19**, 610–616 (2020).
39. Martin, J. et al. Localization of fractionally charged quasi-particles. *Science* **305**, 980–983 (2004).
40. Kastner, M. The single electron transistor and artificial atoms. *Ann. Phys.* **9**, 885–894 (2000).

Methods

Disclination defects

The C_4-symmetric HOTI metamaterials in this study are based on a simple tight-binding model where each unit cell contains four atoms. Each atom is strongly bonded to its nearest neighbours in adjacent unit cells, as shown in Extended Data Fig. 1a, and is weakly bonded to its nearest neighbours within the same unit cell. This HOTI has four bulk bands separated by two bandgaps (the central two bands are degenerate), gapped edge bands and topological corner states[11,41,42]. Most importantly for our study, at 1/4 filling (that is, only the lowest-energy bulk band is filled) the HOTI exhibits a fractional charge of 1/2 at edges and 1/4 at the corners[10,11].

The creation of disclination defects through a 'cutting and gluing' procedure is illustrated in Extended Data Fig. 1 for the HOTI described above, for disclinations with both negative and positive Frank angles. First, the lattice is cut into four identical sectors, which is always possible due to the C_4 symmetry. As the bulk of these sectors is identical to the original insulator, each sector also has a 1/2 edge fractional charge and 1/4 corner fractional charge. A disclination defect with a negative Frank angle can be formed by removing one sector and then gluing the three remaining pieces back together, forming a nominally triangular shape (Extended Data Fig. 1b). The Frank angle Ω can be calculated by drawing a closed loop around the disclination, as illustrated in the schematic of Extended Data Fig. 1b (red arrows). Here a closed loop around the defect needs only three 90° turns, one less than a closed loop in a defect-free lattice, giving a negative Frank angle $\Omega = -90°$. A disclination with a positive Frank angle can be formed by adding one sector, forming a pentagonal shape (Extended Data Fig. 1c). In this case, a closed loop around the defect requires five 90° turns, giving a positive Frank angle $\Omega = +90°$. We note that although the HOTI has non-zero electric polarization at 1/4 filling, the contribution to fractional charge from the second term in equation (1) is zero for both disclinations; both are characterized by the same Burgers vector. We therefore expect the trapped charge at the disclinations to be directly proportional to their Frank angle.

When all four sectors are combined, the fractional boundary charges sum to an integer everywhere within the bulk, leaving a uniform integer charge density. However, at disclination defects, an odd number of sectors are combined, leading to leftover fractional charge at the disclination core. The necessity for this leftover charge can also be seen from the exterior of the system, which has only three (or five) exterior corners due to the defect. In general, the total charge of any insulator must take an integer value as the number of filled states is always an integer. Here, because each corner carries a 1/4 fractional charge, the odd number of corners contributes an overall fractional charge of ±1/4 to the insulator, which can only be compensated by a 1/4 fractional charge in the bulk. We note this 1/4 fractional charge trapped by the disclinations is a feature unique to higher-order topological insulators[11], as the first-order features in C_4 symmetric TCIs, namely the polarization and related edge fractional charge, are always quantized in units of 1/2.

Design of microwave-frequency metamaterials

We physically realize the HOTIs with disclination defects in metamaterials consisting of coupled microstrip resonators, each with a fundamental resonance frequency $f_0 \approx 2.6$ GHz and a quality factor of about 160. Each resonator corresponds to an atom, or a single degree of freedom, and the resonators are coupled by discrete capacitors that correspond to the bonds between atoms. The fabricated microwave-frequency metamaterials with negative and positive disclination angles are shown in Extended Data Fig. 1d, e, respectively. Note that the physical coupling within the bulk forms a symmetric square in both metamaterials, as shown in the insets of Extended Data Fig. 1d, e and schematically in Extended Data Fig. 1b, c, except at the centre of each board. To preserve this square coupling region, which helps to ensure equal coupling rates between resonators, the shapes of the individual resonators become distorted towards the edges of the board. Nevertheless, all resonators are designed to have the same electric length and as such have the same fundamental resonance frequency of 2.6 GHz. The metamaterials are also designed to have an overall C_3 or C_5 symmetry, as this global rotation symmetry fixes the total fractional mode density in each symmetric sector.

The metamaterials are fabricated on 0.787-mm-thick Rogers RT/duroid 5880 substrate, with 35-μm-thick copper on each side. The resonators that make up each metamaterial are half-wavelength microstrip transmission lines, with a characteristic impedance of each section $Z_0 \approx 110\ \Omega$. The resonator layout is such that the coupling between resonators forms a square (Extended Data Fig. 1), requiring that the resonator shape changes slightly from the centre of each board to the outside. To keep the electrical length of each resonator approximately equal, the resonators have a curved section in their centre, where the curvature decreases away from the centre of the C_3-symmetric board, and increases away from the centre of the C_5-symmetric board. Although there are losses in both the dielectric substrate and the copper conductor, as well as comparatively negligible radiative losses, these are small (the typical resonator linewidth is about 16 MHz, for a typical quality factor of about 160) and do not affect the underlying topology. The coupling between resonators is implemented using two discrete capacitors in series, such that the strong coupling capacitance is 0.3 pF (two 0.6-pF capacitors), and the weak coupling capacitance is 0.05 pF (two 0.1-pF capacitors).

Measuring electric charge equivalent via density of modes in a microwave metamaterial

The metamaterials studied here are neutral bosonic systems and do not carry literal electric charge; instead, reflection spectroscopy can be used to measure their local DOS directly with high spatial resolution. By integrating the measured DOS over the frequency range of an entire bulk band, and normalizing to correctly count the number of modes in each unit cell, an analogous quantity to the charge density can be determined as if each state of the bulk band were filled by a single electron. This analogous quantity physically represents the density of modes, or the mode density, in a unit cell over a given frequency range. Previous work has shown that measurements of mode density successfully capture previously inaccessible observables such as fractional corner charge, and can be used to identify both first-order and higher-order topology in TCIs[11].

We experimentally find the local DOS of the microwave metamaterials by first measuring the reflection spectrum $S_{11}(f)$ at each resonator, where f is the frequency. The reflection measurements are taken using a microwave network analyser (Keysight E5063A). The reflection probe is composed of a 50-Ω coaxial cable terminated in a 0.1-pF capacitor, which is contacted to each resonator at an anti-node. Owing to the low probe capacitance, the measured linewidths are dominated by intrinsic losses in each resonator. The background reflection contributed by the probe is evaluated away from any modes and is removed. This measurement process is similar to that used in ref. [43].

The absorptance $A(f)$, which is defined as the ratio of absorbed power to incident power, can be calculated from the reflection as $A(f) = 1 - |S_{11}(f)|^2$. To obtain the DOS $D(f)$ for each resonator, we divide the measured absorptance by the frequency squared, $D(f) = A(f)/f^2$, which accounts for increased coupling to the capacitive probe at higher frequencies. Finally, we normalize $D(f)$ such that

$$\int_{\text{All bands}} D_{\mathbf{r}}(f) = 1,$$

where the integration is over the whole band structure and $D_{\mathbf{r}}(f)$ is the local DOS for one resonator, indexed by the resonator number $\mathbf{r}$. As each resonator supports a single mode within the measured frequency

range, such that for an N-resonator system there are N modes in total, this normalization maps each mode to a mode density of 1.

Index of fractional disclination charge

In this section, we describe in detail the quantities in equation (1). We also discuss why the fractional charges trapped by the disclinations studied in the main text are proportional to their Frank angle.

A disclination defect is characterized by the amount of net translation (denoted by the Burgers vector **B**) and net rotation (denoted by the Frank angle Ω) accumulated under parallel transport of a vector along a loop enclosing the disclination core. To illustrate these two quantities, we consider a C_4-symmetric square lattice with a disclination defect at the centre. As shown in Extended Data Fig. 2a, the lattice vectors are denoted by $\mathbf{e}_1$ and $\mathbf{e}_2$. The vector $\mathbf{v}$ is parallel transported along the loop ABCA that encloses the disclination core, meaning that the vector is translated around the loop by an integer number of lattice vectors with a 90° rotation at each corner. Compared with the same transport conducted in a perfect lattice without defects, which is shown in the inset of Extended Data Fig. 2a, we find that after enclosing the disclination core, the final vector has gained an extra rotation of −90°, and an extra translation of $2\mathbf{e}_2$, corresponding to $\Omega = -90°$, $\mathbf{B} = 2\mathbf{e}_2$. In two-dimensional C_4-symmetric lattices, the parity of the sum of the Burgers vector components classifies disclinations with the same Frank angles[28], such that for a fixed Frank angle there are only two types of topologically distinct disclination. In type-I disclinations, the sum of the Burgers vector components is even, as shown in Extended Data Fig. 2a. A type-II disclination, where the extra translation accumulated after looping around the disclination core is $1\mathbf{e}_2$, is shown in Extended Data Fig. 2b.

The two different types of disclination trap different fractional charges, even if they have the same Frank angle. As shown recently[14], one can find the fractional disclination charge by inspecting the real-space localized Wannier representation of an insulator. The representation corresponding to the C_4-symmetric HOTI studied in the main text has a single Wannier centre at the corner of a unit cell (Wyckoff position b), which generates a bulk polarization $\mathbf{P} = 1/2(\mathbf{e}_1 + \mathbf{e}_2)$ (we set the charge $e = 1$). Owing to the C_4 symmetry, the single Wannier centre at the unit cell corner contributes an equal quantized fractional charge of 1/4 to each of the adjacent four unit cells. In Extended Data Fig. 2c, d, we show how the bulk Wannier centres are arranged around both type-I and type-II disclinations. For the lattice with a type-I disclination, the unit cell at the core receives contributions from three Wannier centres, leading to a fractional charge of 3/4. In contrast, for the lattice with a type-II disclination, each of the three unit cells around the disclination core manifests a fractional charge of 3/4, leading to a total fractional disclination charge of 9/4 mod 1 = 1/4.

In addition to the corner of the unit cell (Wyckoff position b), Wannier centres in a C_4-symmetric insulator are allowed at all the positions shown in Extended Data Fig. 2e. For these more general cases, the index of fractional disclination charge in C_4-symmetric insulators is[14]

$$Q_{\mathrm{dis}} = \frac{\Omega}{2\pi}(n_b + 2n_c) + \sum_{i,j=1,2} \epsilon_{ij} B_i P_j \ \text{modulo}\ 1 \qquad (2)$$

where n_b and n_c are the number of Wannier centres located at the Wyckoff positions c and b, respectively, which are determined by the band topology of the insulator; B_i and P_i are the component of the Burgers vector and the bulk polarization, respectively; and $\epsilon_{ii} = 0$, $\epsilon_{ij} = -\epsilon_{ji} = 1$. Notice that for type-I disclinations in C_4-symmetric insulators, as the sum of components of the Burgers vector is always even and $P_1 = P_2$, the second term in equation (2) always gives an integer number. Therefore, the fractional disclination charge index for the type-I disclination is

$$Q_{\mathrm{dis,\ type\text{-}I}} = \frac{\Omega}{2\pi}(n_b + 2n_c) \ \text{modulo}\ 1. \qquad (3)$$

Therefore, the fractional charge trapped at the disclination core for a given band structure is only proportional to the Frank angle Ω, which is consistent with our experimental measurement.

Spectral flow of topological bound states

In this section, we take the deformed triangular HOTI that is measured in the main text as an example to illustrate the unique behaviour of the topological bound states when local on-site potentials are applied. As we will show, without chiral symmetry the energy of the topological bound states is given by the on-site energy of the site where they are localized.

The lattice configuration of the triangular C_4-symmetric HOTI is shown in Extended Data Fig. 3a. We apply an on-site potential to an interior corner site (hosting a topological bound state) and a bulk site, marked by the red and green circles in Extended Data Fig. 3a, respectively. In Extended Data Fig. 3b, we show the simulated spectrum as a function of the on-site potential for both sites. The topological bound state moves approximately linearly across the entire band structure as the on-site potential is tuned. This transfer of a mode between bulk bands, which resembles a topological pumping process, is a characteristic feature of topological bound states.

In contrast, for the bulk site, we observe an avoided crossing of the localized mode with the band structure. We can pull a mode from the lower bulk band below the band structure when a large negative on-site potential is applied, or pull a mode from the upper bulk band above the band structure with a large positive on-site potential. However, a mode cannot be transferred between bands across the entire bulk bandgap.

As a further comparison, in Extended Data Fig. 3c, we show the simulated spatial distribution of the emergent in-gap modes for both the topological bound state and the de-tuned bulk site. In both cases, the in-gap mode is localized at the position of the applied on-site potential, but this localization alone does not qualify these modes as topological bound states. For the de-tuned bulk site, the in-gap mode is distributed among four neighbouring bulk sites and not confined to one sublattice, indicating a topologically trivial defect state. In the topological phase, the in-gap mode is confined to the same sublattice site in bulk and edge unit cells, indicating a topological state that is supported by the bulk.

Effects of removing sites from the lattice

In this section, we show through simulations that removing a site from the lattice will not change the total fractional mode density, but can remove topological bound states. Let us consider the same C_4-symmetric HOTI as studied in the main text, the lattice configuration of which is shown (with no defects) in Extended Data Fig. 4a, d. To mimic our experiments, we intentionally do not compensate the intrinsic capacitive loading effect[11], which shifts the energy of the bulk bands down in relation to the energy of the topological corner states (Extended Data Fig. 4b, e). The resulting system has three bands as shown in Extended Data Fig. 4b, e, and can be divided into four identical sectors due to the C_4 symmetry. The singly degenerate bands, band 1 and band 3, manifest a fractional mode density of 1/4 in each sector, while the doubly degenerate band 2 manifests that of 1/2 per sector.

To simulate removing a site adiabatically, we apply an increasing on-site potential to that site. We first consider detuning the resonator at the top-right corner, which hosts a localized topological corner mode. As shown in Extended Data Fig. 4b, the corner mode is lifted and separated from the band structure as the on-site potential increases and the corner site is effectively removed from the lattice. However, it is evident from Extended Data Fig. 4c that the fractional part of mode density in each band, integrated over the whole top-right sector, remains constant through the whole process. This occurs because an integer number of modes are removed from that sector, such that the mode density can only change by an integer number. Furthermore,

the fractional part of the total mode density is a collective behaviour of all modes in the band, and with only nearest-neighbour couplings, a local deformation does not affect the mode density in the areas far away from that deformation.

We also consider removing a bulk resonator in the top-right sector, and the resulting spectrum and sector fractional mode density are shown in Extended Data Fig. 4e, f. As before, one mode, localized where the on-site potential is applied, is dragged out of the band structure while the integrated fractional mode density in the top-right sector remains the same. In addition, note that this deformation introduces one mode into the bandgap, thereby creating an in-gap bound state despite not changing the fractional mode density.

Simulations for large systems

In Extended Data Figs. 5, 6, we present tight-binding simulations of the fractional mode density for larger versions (15 unit cells per side) of the crystalline insulators studied in the main text. These simulations confirm our experimental findings that disclination defects can robustly trap fractional charges and this trapped charge can indicate non-trivial, higher-order crystalline topology even in the absence of any spectral signatures.

Detailed experimental figures

We present detailed versions of the experimental figures in the main manuscript as Extended Data, showing explicitly the total measured mode density for each unit cell. The data in Fig. 1 are shown in Extended Data Figs. 7, 8, the data in Fig. 2 are shown in Extended Data Fig. 9, and the data in Fig. 3 are shown in Extended Data Fig. 10.

Data availability

The data that support the findings of this study are available from the authors on reasonable request.

41. Mittal, S. et al. Photonic quadrupole topological phases. *Nat. Photon.* **13**, 692–696 (2019).
42. Liu, S. et al. Topologically protected edge state in two-dimensional Su–Schrieffer–Heeger circuit. *Research* **2019**, 8609875 (2019).
43. Peterson, C. W., Benalcazar, W. A., Hughes, T. L. & Bahl, G. A quantized microwave quadrupole insulator with topologically protected corner states. *Nature* **555**, 346–350 (2018).

Acknowledgements The authors thank J. T. Bernhard for access to the resources at the UIUC Electromagnetics Laboratory. This project was supported by the US National Science Foundation (NSF) Emerging Frontiers in Research and Innovation (EFRI) grant EFMA-1641084 and by the US Office of Naval Research (ONR) Multidisciplinary University Research Initiative (MURI) grant N00014-20-1-2325 on Robust Photonic Materials with High-Order Topological Protection. C.W.P. additionally acknowledges support from the NSF Graduate Research Fellowship. G.B. additionally acknowledges support from the ONR Director for Research Early Career Grant N00014-17-1-2209. T.L. and T.L.H. additionally thank the US National Science Foundation under grant DMR-1351895.

Author contributions C.W.P. designed and fabricated the microwave circuits, performed the microwave simulations and experimental measurements, and produced the experimental figures. W.J. assisted with the microwave circuit design and experimental measurements. T.L. guided the topological insulator design and performed the theoretical calculations. T.L.H. and G.B. supervised all aspects of the project. All authors jointly wrote the paper.

Competing interests The authors declare no competing interests.

Additional information
Correspondence and requests for materials should be addressed to G.B.
Peer review information *Nature* thanks Carmine Ortix and the other, anonymous, reviewer(s) for their contribution to the peer review of this work.
Reprints and permissions information is available at http://www.nature.com/reprints.

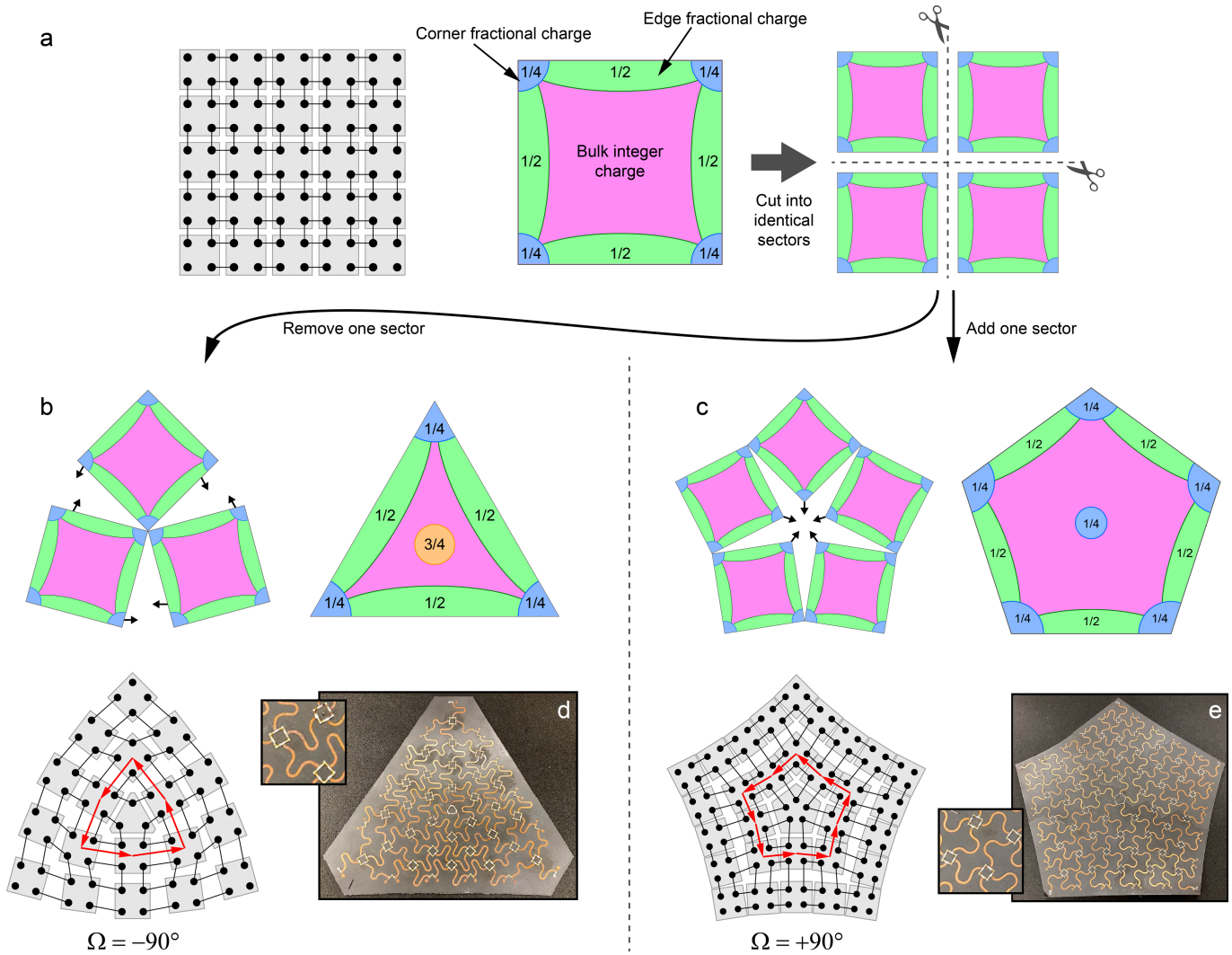

Extended Data Fig. 1 | Fractional charge at disclination defects. **a**, C_4-symmetric HOTI with 1/4 corner charge and 1/2 edge charge. A schematic of the tight-binding model (black dots are atoms, black lines are strong bonds) and illustration of the fractional charge are shown. Owing to its C_4 symmetry, the HOTI can be cut into four identical sectors. **b**, One sector is removed and the remaining three are glued together to create a disclination defect with a negative Frank angle $\Omega = -90°$. Red arrows on the schematic show calculation of the Frank angle. The disclination traps a 3/4 fractional charge, as it is formed by combining three 1/4 charge corners. **c**, One sector is added and the resulting five are glued together to create a disclination defect with a positive Frank angle $\Omega = +90°$. Red arrows on the schematic show calculation of the Frank angle. The disclination traps a 1/4 fractional charge, as it is formed by combining five 1/4 charge corners. **d**, Photo of fabricated microwave-frequency circuit topological insulator with disclination having a Frank angle $\Omega = -90°$. **e**, Photo of fabricated circuit with disclination having a Frank angle $\Omega = +90°$. Insets show C_4-symmetric bulk coupling.

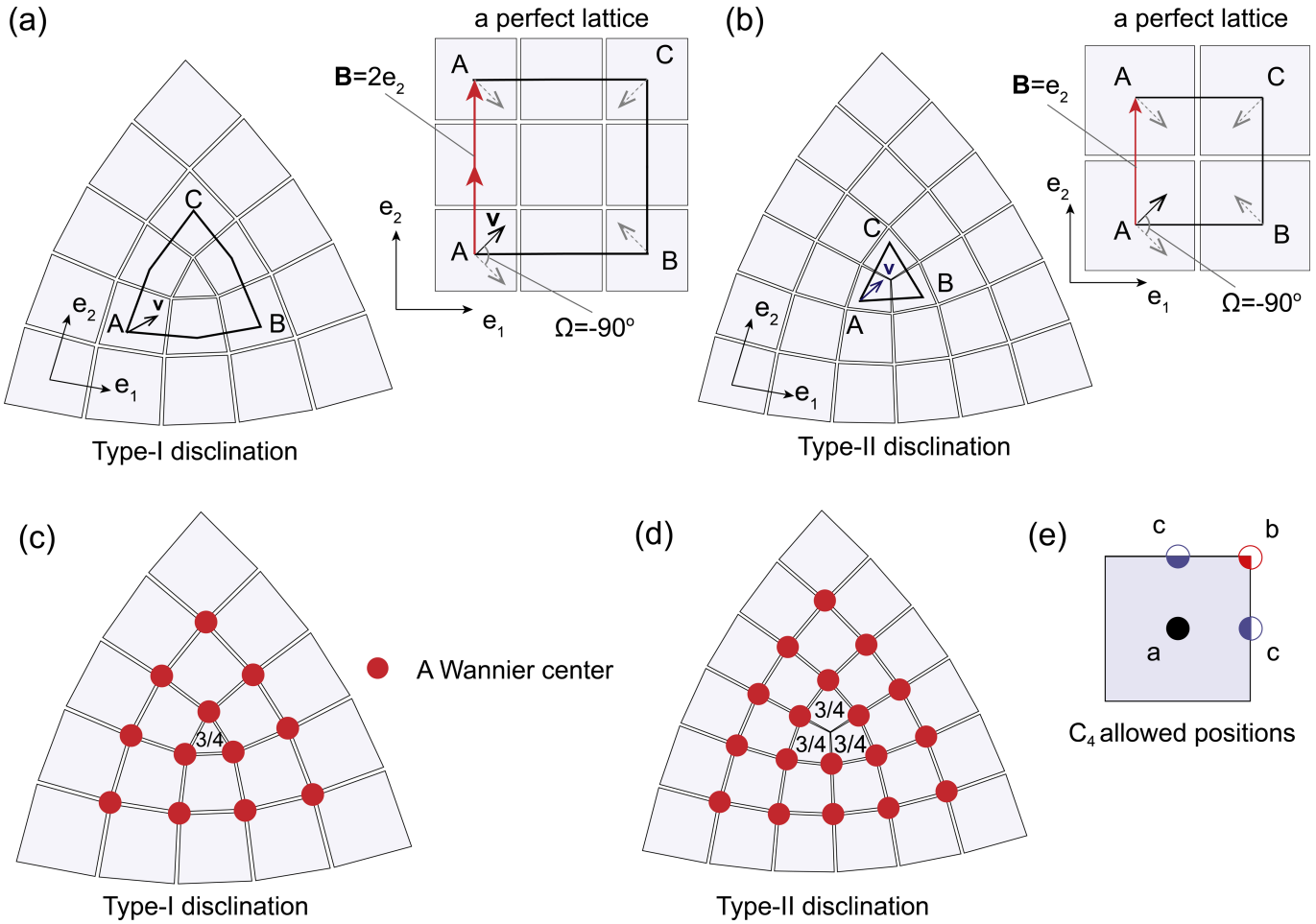

Extended Data Fig. 2 | Burgers vector and Frank angle of disclinations. **a**, **b**, Demonstration of calculating the Burgers vector and Frank angle for a C_4-symmetric square lattice with the type-I disclination (**a**) and type-II disclination (**b**). The black arrows indicate the vector being parallel transport enclosing the disclination core and the dashed grey arrows indicate that vector in the process of the parallel transport. **c**, **d**, The Wannier centre configuration and fractional charge in defective lattices with the type-I disclination (**c**) and type-I disclination (**d**). **e**, Allowed positions of Wannier centres by the C_4 symmetry in one unit cell.

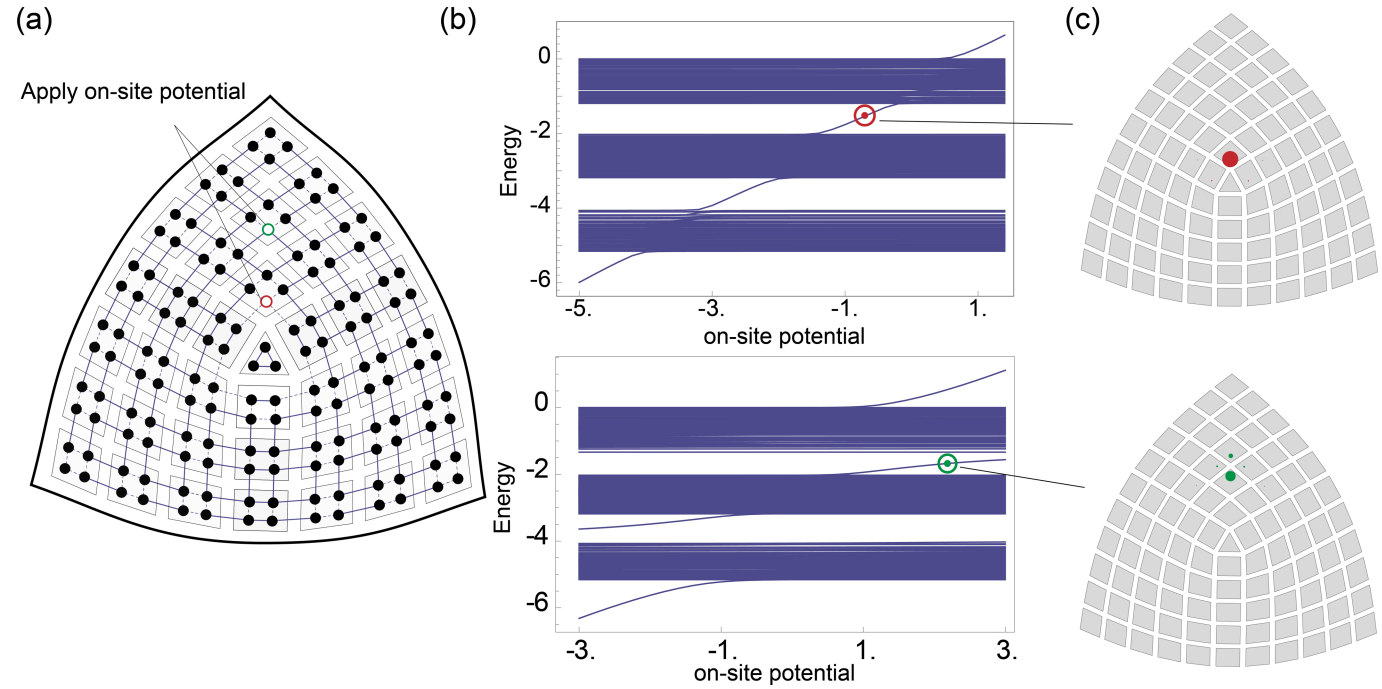

Extended Data Fig. 3 | Spectral flow of topological bound states. **a**, Schematic of the lattice configuration for the C_3 symmetric TCI. t_0 and t indicate the intracell coupling strength and intercell coupling strength, respectively. We apply an on-site potential to the bottom-left corner site. **b**, The spectrum of the C_3 TCI as a function of on-site potential α for a topological phase with $t = 1.0$ and $t_0 = 0.5$ (top) and a trivial phase with $t = 0.5$ and $t = 1.0$ (bottom). The red line represents energy shift of the corner mode. **c**, The spatial distribution of the in-gap mode (encircled in **b**) over the bottom-left corner of the lattice. We use $\alpha = -1$ for the topological phase and $\alpha = 1$ for the trivial phase. The simulation is conducted on a triangle lattice with 15 unit cells per side.

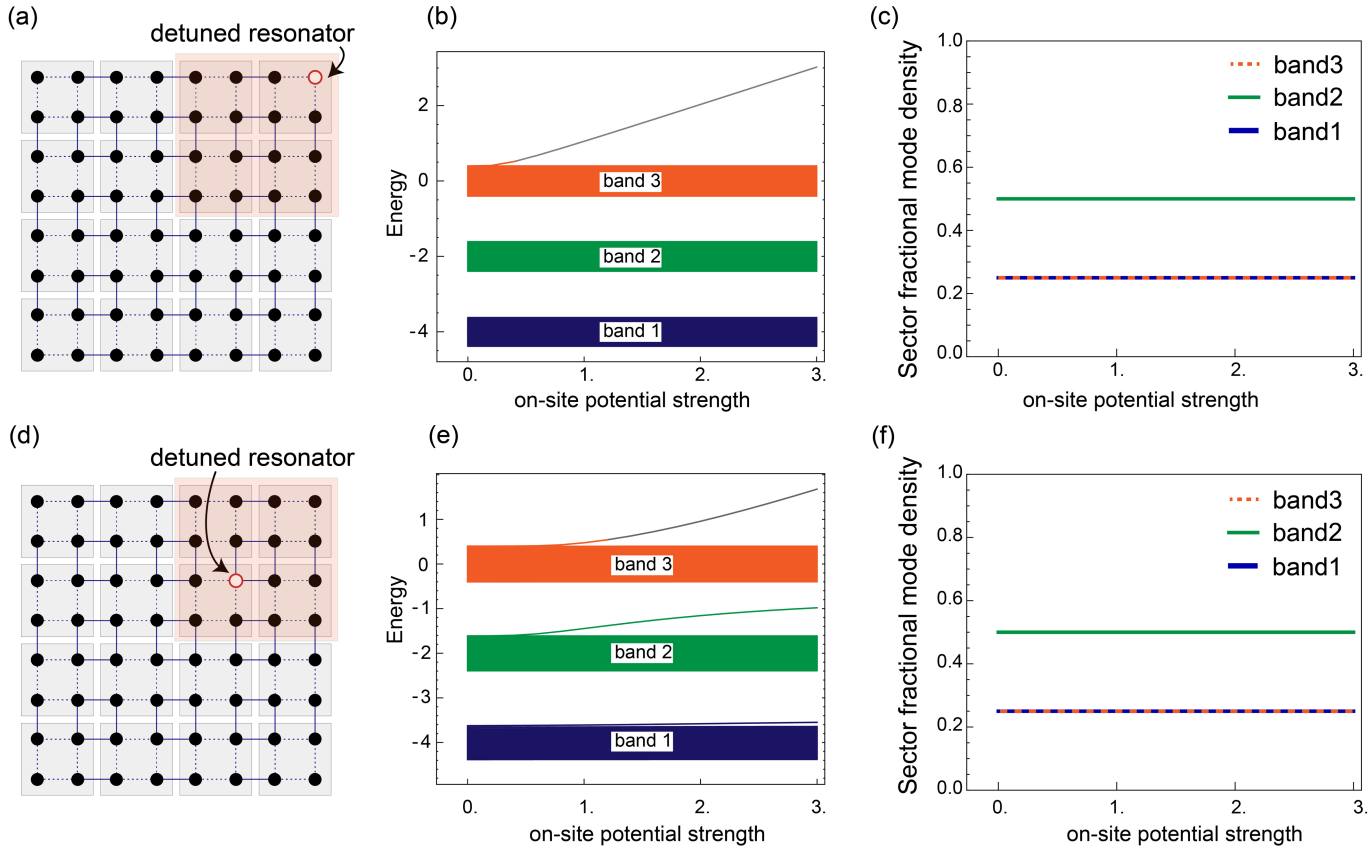

Extended Data Fig. 4 | Removing lattice sites. a, **d**, Lattice configuration of the HOTI used in simulations. We consider a lattice with 10 × 10 unit cells, intracell coupling strength of 0.25 (dashed lines) and intercell coupling strength of 1 (solid lines). The resonator being removed is denoted by a red circle. **b**, **e**, The spectrum of the lattice in **a** and **d** as a function of the on-site potential applied to the highlighted resonators. **c**, **f**, The fractional part of the mode density integrated over the shaded sector in **a** and **d** for each band.

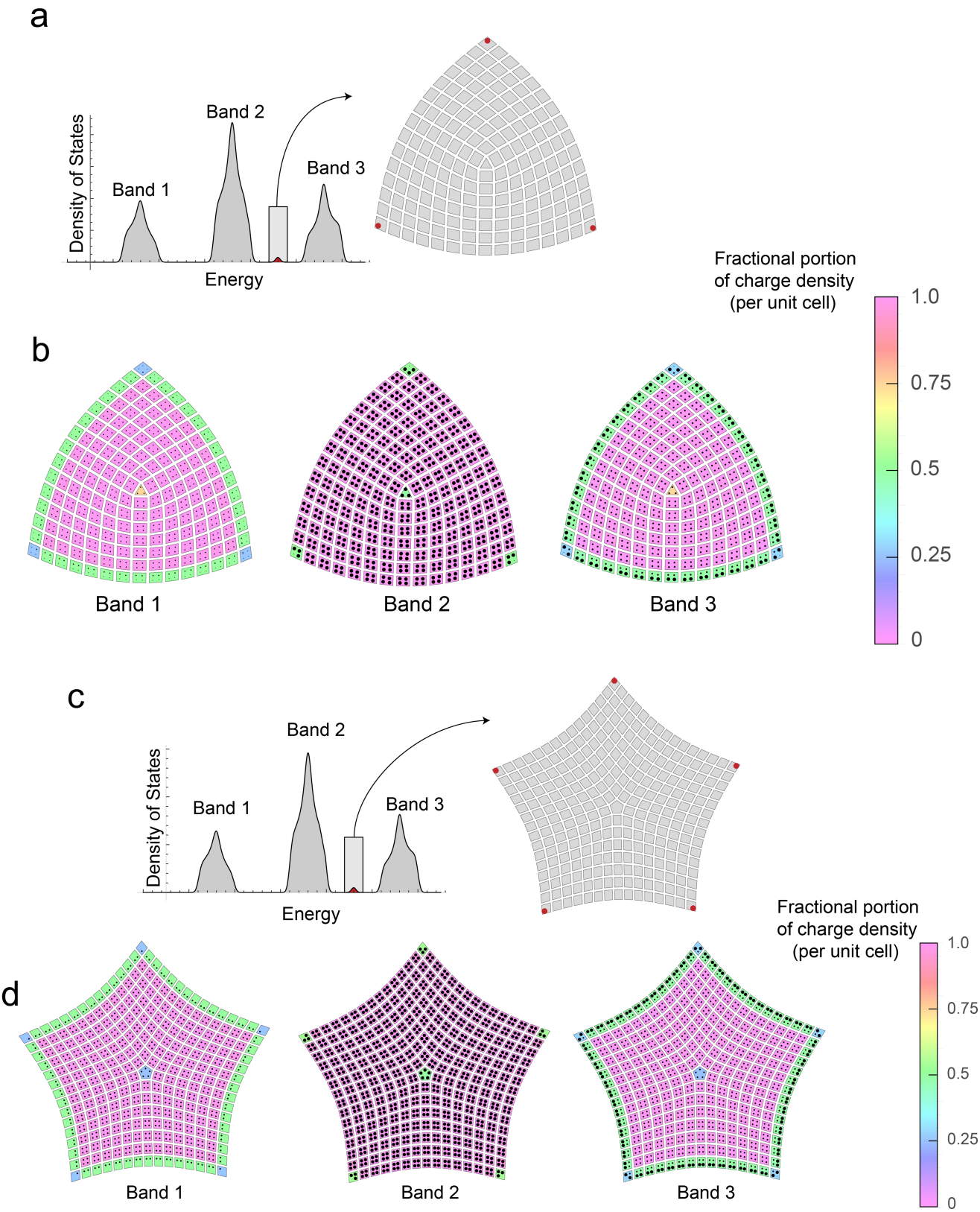

Extended Data Fig. 5 | Fractional mode density in large systems. Tight-binding simulation of fractional mode density in large systems (15 unit cells per side) with Frank angles $\Omega = \pm 90°$. We set the intercell coupling strength to be 1 and intracell coupling strength to be 0.2. **a**, Simulated DOS spectrum and real-space distribution of in-gap modes for a Frank angle $\Omega = -90°$. On-site potentials are applied to the corner sites to pull the corner states into the bulk bandgap. **b**, Fractional portion of the mode density for each band. The colour of each unit cell indicates the fractional portion of mode density in that cell, and the area of each dot is proportional to the mode density of the corresponding resonator. The fractional part of the integrated mode density around the central unit cell is 3/4 for bands 1 and 3 and 1/2 for band 2. **c**, **d**, Same as **a** and **b** but for Frank angle $\Omega = +90°$. The fractional part of the integrated mode density around the central unit cell is 1/4 for bands 1 and 3 and 1/2 for band 2.

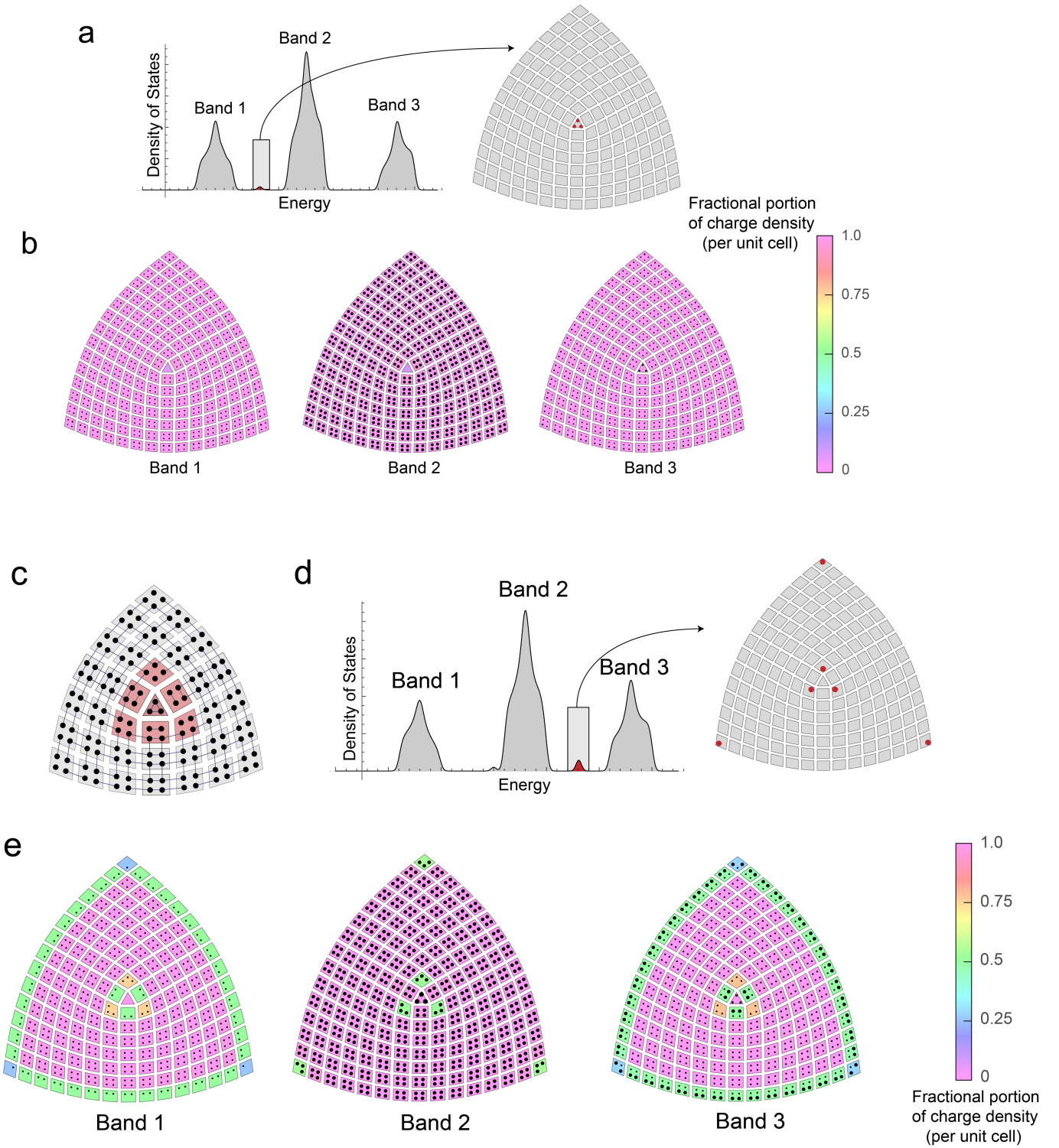

Extended Data Fig. 6 | Fractional mode density in large trivial and deformed systems. a, **b**, Tight-binding simulation of fractional mode density in large topologically trivial system (15 unit cells per side) with a Frank angle $\Omega = -90°$. We set the intercell coupling strength to be 0.2 and intracell coupling strength to be 1. **a**, Simulated DOS spectrum and real-space distribution of in-gap modes. The in-gap modes are localized within the central defective unit cell, which only has three sites. **b**, Fractional portion of the mode density for each band. The mode density takes an integer value in all unit cells. **c**–**e**, Tight-binding simulation of fractional mode density in a large system (15 unit cells per side) with a Frank angle $\Omega = -90°$ and with the central unit cell trivialized. We set the intercell coupling strength to be 1 and intracell coupling strength to be 0.2. **c**, Schematic of deformed lattice with trivialized central unit cell. **d**, Simulated DOS spectrum and real-space distribution of in-gap modes. On-site potentials are applied to the corner sites as well as the 'interior corners' to pull six topological bound states into the bulk bandgap. **e**, Fractional portion of the mode density for each band. The colour of each unit cell indicates the fractional portion of mode density in that cell, and the area of each dot is proportional to the mode density of the corresponding resonator. The fractional part of the integrated mode density around the central unit cell remains 3/4 for bands 1 and 3 and 1/2 for band 2.

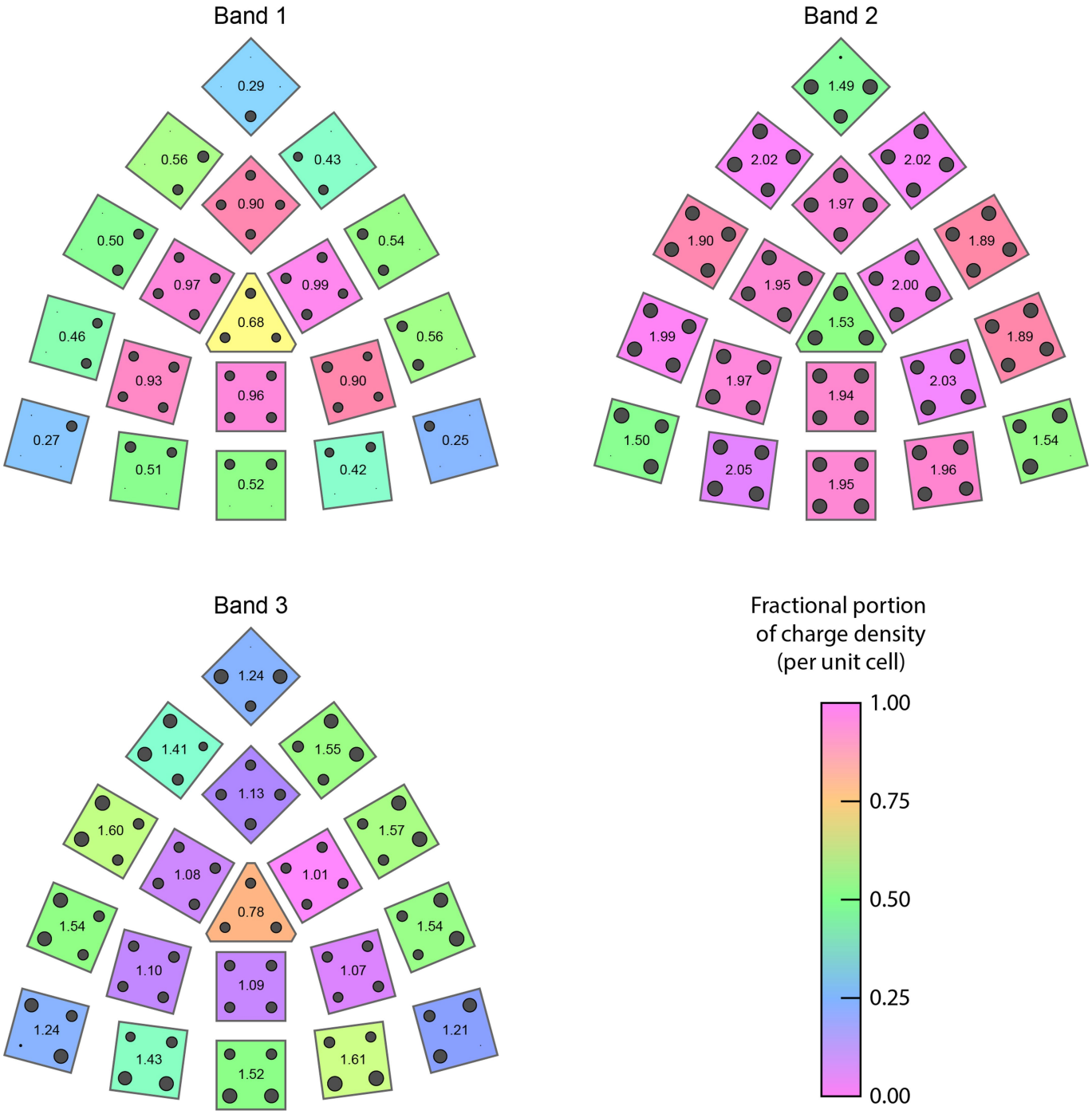

Extended Data Fig. 7 | Detailed mode density for the C_3-symmetric insulator. Measured mode density for the C_3-symmetric insulator, as shown in Fig. 1c. The total mode density for each band is listed numerically in each unit cell, and the area of each dot is proportional to the mode density of the corresponding resonator. The colour of each unit cell indicates the fractional portion of mode density.

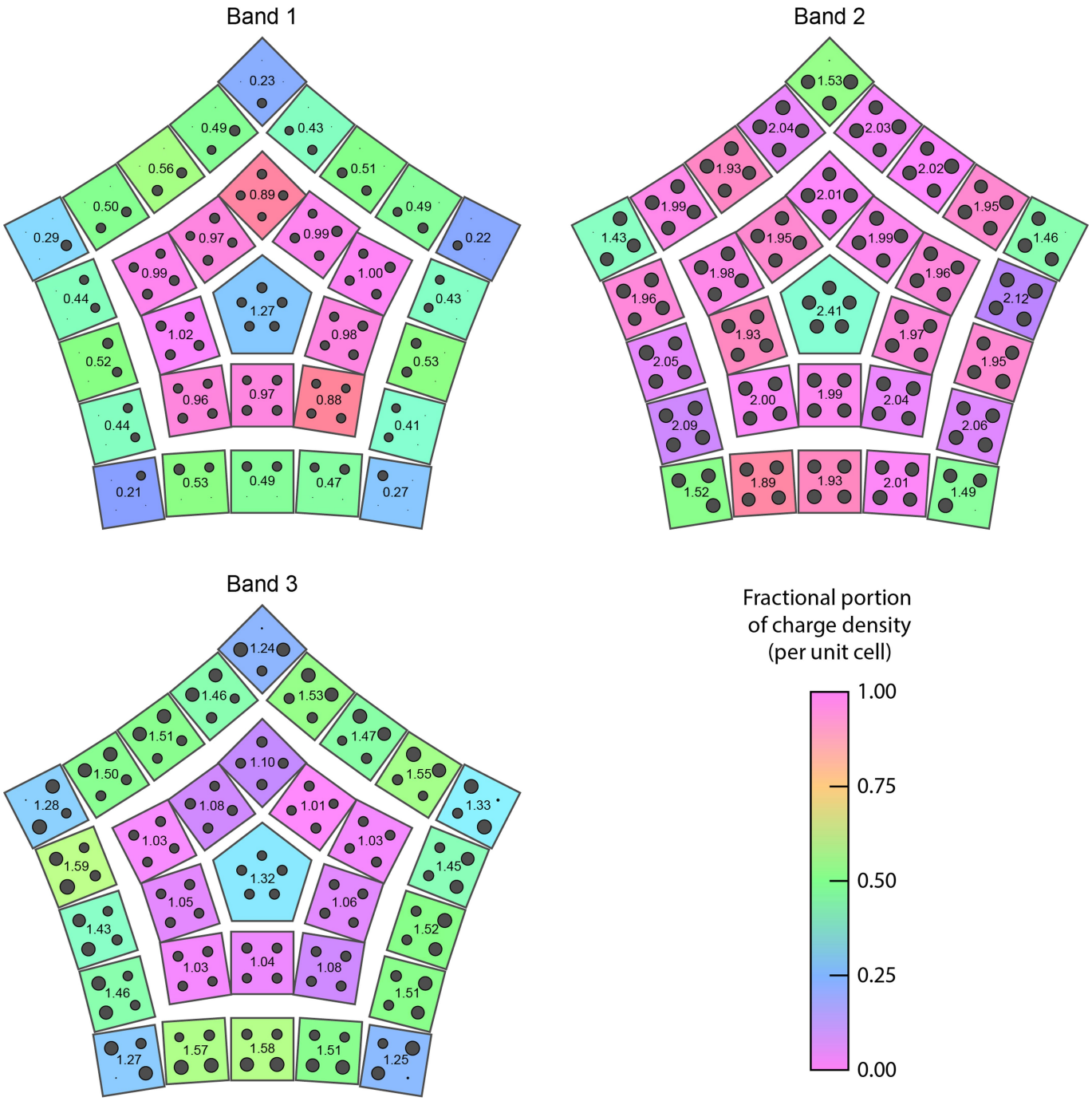

Extended Data Fig. 8 | Detailed mode density for the C_5-symmetric insulator. Measured mode density for the C_5-symmetric insulator, as shown in Fig. 1d. The total mode density for each band is listed numerically in each unit cell, and the area of each dot is proportional to the mode density of the corresponding resonator. The colour of each unit cell indicates the fractional portion of mode density.

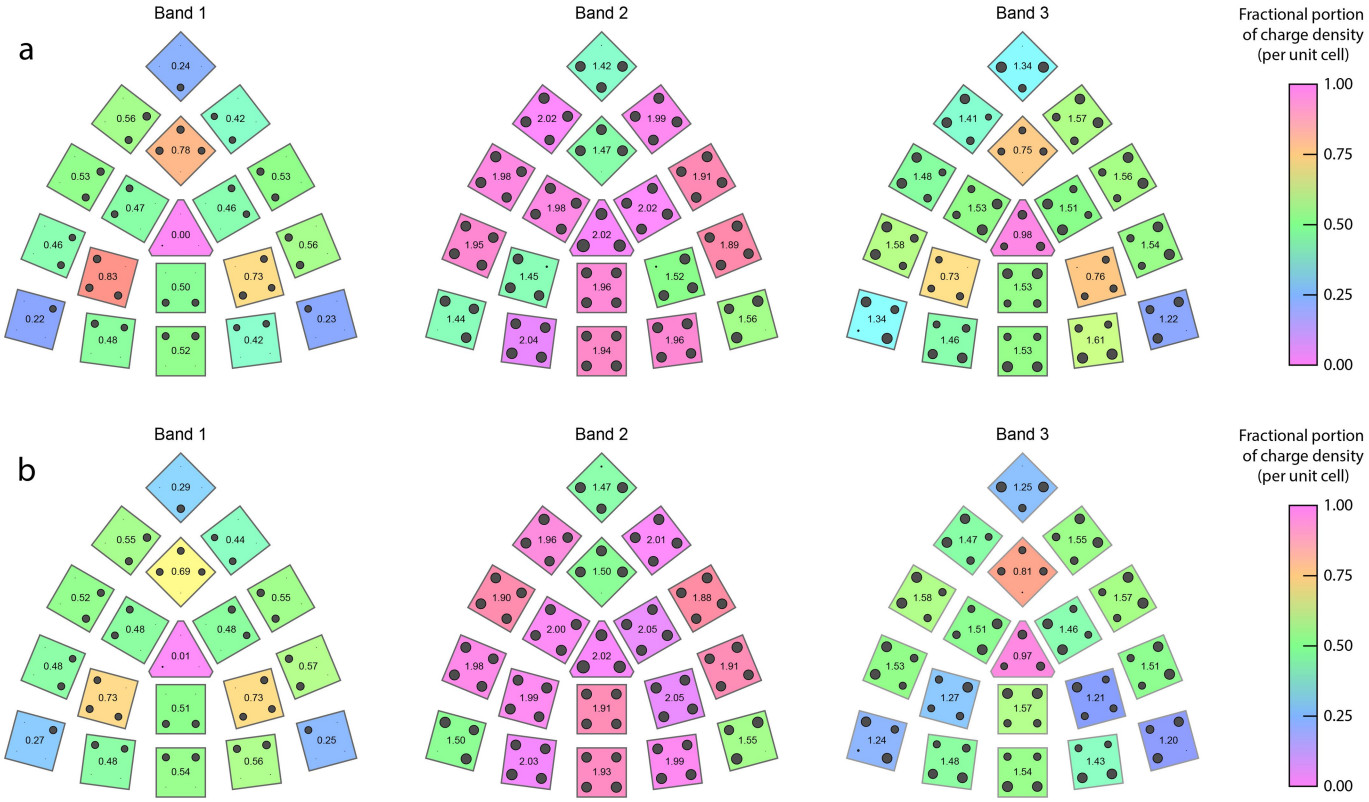

Extended Data Fig. 9 | Detailed mode density for deformed C_3-symmetric insulator. a, Measured fractional mode density for the C_3-symmetric insulator after the central unit cell is trivialized, as shown in Fig. 2c. The total mode density for each band is listed numerically in each unit cell, and the area of each dot is proportional to the mode density of the corresponding resonator. The colour of each unit cell indicates the fractional portion of mode density. **b**, Same as **a** but with broken rotation symmetry as in Fig. 2f.

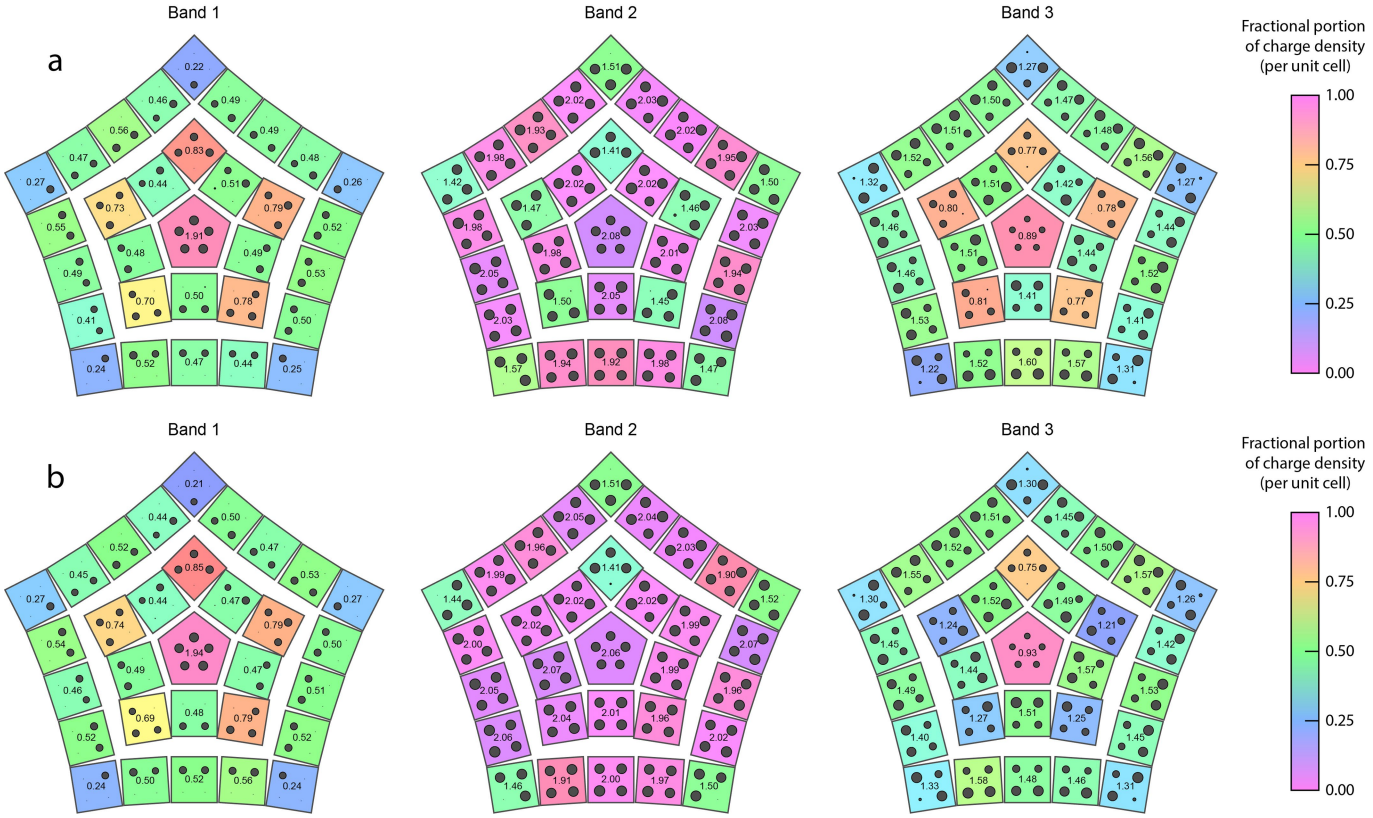

Extended Data Fig. 10 | Detailed mode density for deformed C_5-symmetric insulator. a, Measured fractional mode density for the C_5-symmetric insulator after the central unit cell is trivialized, as shown in Fig. 3c. The total mode density for each band is listed numerically in each unit cell, and the area of each dot is proportional to the mode density of the corresponding resonator. The colour of each unit cell indicates the fractional portion of mode density. **b**, Same as **a** but with broken rotation symmetry as in Fig. 3f.